SIMULTANEOUS MEASUREMENTS OF SURFACE TOPOGRAPHY AND VELOCITY FIELDS ON BOTH SIDES OF A GAS–LIQUID INTERFACE

Petter R. Benonisen†, Srikar Yadala, Leon Li, Ali Semati, Simen Å. Ellingsen, and R. Jason Hearst
Department of Energy and Process Engineering
Norwegian University of Science and Technology
Kolbjørn Hejes vei 2, 7034 Trondheim, Trøndelag, Norway
†petter.r.benonisen@ntnu.no

ABSTRACT

The two-point velocity correlations of the airflow above a moving air–water interface in a channel flow are investigated experimentally using stereo particle image velocimetry (SPIV) in horizontal planes above and below the surface simultaneously. Surface topography is captured in tandem with SPIV measurements using profilometry. An active grid, moving independently in both phases, allows one to tailor the freestream turbulence and vary it systematically. In the gas-phase, long meandering, low-momentum structures reminiscent of log-region boundary layer streaks are found. The streamwise velocity correlations confirm their likeness, growing with the freestream Reynolds number. In addition to an expected increase in surface deformation amplitude and wavelength with gas-phase Reynolds number, Re_M, changing the freestream turbulence intensity, $(u'/U)_0$, has a considerable effect. On the other hand, the spanwise and vertical velocity correlations' dependence on freestream parameters differs from that of turbulent boundary layers. Especially, the vertical velocity correlations show high surface wave coherence, growing in both streamwise and spanwise directions as the freestream velocity and turbulence intensity (and thus surface deformation wavelength) increase.

INTRODUCTION

The oceans function as a planetary heat and carbon sink. About 56 % of anthropogenic CO_2 emissions are sequestered annually, making the oceans the largest carbon sink by a wide margin (IPCC, 2023). The effects of atmospheric and oceanic turbulence on wave generation and subsequently momentum, heat, and gas transport are still an active area of research. In the wind-driven wave regime, the freestream velocity is on the same order of magnitude or higher than the peak wave speed. It has long been an established understanding that, in general, under such conditions, the wave amplitude varies exponentially with time (Miles, 1957) after a short inception period of linear growth (Phillips, 1957; Li & Shen, 2022). And although our understanding of the underlying mechanisms that drive wave growth is incomplete, two main interpretations have been used in modelling with success: namely, the critical-layer model proposed by Miles (1957) and the nonseparated sheltering model of Belcher & Hunt (1998).

The coupling between surface waves and flow fields on both sides of the interface dictates the permitted flow states. For instance, in laboratory experiments with gas-phase velocities and stresses low enough not to generate surface waves, it has been found that the velocity profile adheres to the law of the wall. When waves are generated, either through increased wind speeds or mechanical means, ejections and sweeps become more prevalent (Buckley & Veron, 2016). When the waves have grown sufficiently large compared to the wind speed, gas-phase flow separation past the wave crest may occur and has been documented for moving wavy interfaces as well as wavy solid walls (Shaikh & Siddiqui, 2010). Separation events create significant reductions in tangential surface stress past the wave crest, leading to intense wave-turbulence coherence. The sheltering effects arising from separation events have been found to extend over one or more wavelengths, intermittently merging with one another and breaking apart (Tondu *et al.*, 2025). As wave age increases and waves transition into micro-breaking and breaking regimes, separation becomes more prevalent—an effect of breaking being a sufficient, albeit not a necessary condition for separation (Buckley *et al.*, 2020).

On the liquid side of the interface, orbital wave motions dominate the velocity fields, with higher longitudinal velocities under wave crests and lower velocities under troughs. Turbulence levels and dissipation rates can reach magnitudes far exceeding those observed near solid walls in similar shear stress conditions (Thais & Magnaudet, 1996), an effect which is significantly enhanced by wave breaking (Agrawal *et al.*, 1992). Additionally, parallel series of long counter-rotating vortices known as Langmuir turbulence typically develop (Leibovich, 1983; Veron & Melville, 2001). Coherent structures under wind waves are highly dependent on gas-phase flow velocity and surface topography, whereby maximum vorticity, longitudinal size, diameter and frequency of occurrence all increase with the gas-phase freestream velocity (Siddiqui *et al.*, 2004).

To the authors' knowledge, the impact of freestream turbulence on wave generation and near-interface flow structures is yet to be investigated thoroughly. Therefore, in this study, the interface topography and near-surface velocity fields on both sides of the gas–liquid interface are investigated in a combined air–water channel facility with tailored freestream turbulence generated by active grids. SPIV measurements are obtained at an intermediate acquisition frequency (15 Hz) for the liquid phase simultaneously with high-speed (1 kHz), time-resolved gas-phase SPIV and profilometry measurements. Although the facility permits co-flowing experimental cases, for brevity, the focus is kept to the gas-phase flow in purely wind-driven conditions.

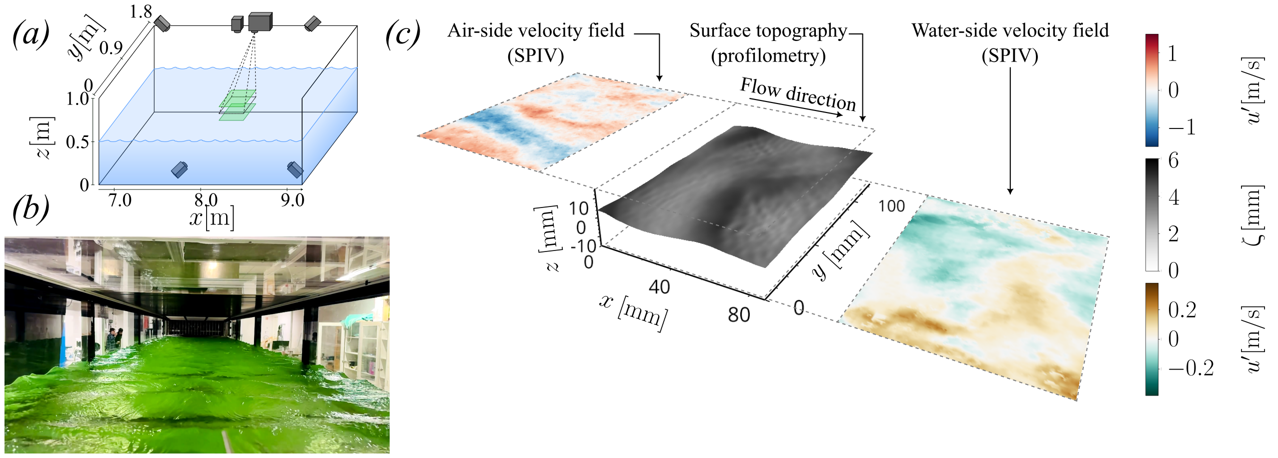

Figure 1. *(a)* Measurement location of test section depicting two SPIV laser sheets, two high-speed and two low-speed cameras together with the projector-camera profilometry setup. *(b)* A photo taken from the downstream end of the test section looking towards the active grid in high-wind conditions. *(c)* Illustration showing the relative locations of the two SPIV measurement planes and the surface topography between them.

EXPERIMENTAL DETAILS

The experimental campaign was conducted in the large water channel at the Norwegian University of Science and Technology's Fluid Mechanics Laboratory. It is a combined wind tunnel and water channel facility with an 11.2 m long (x-direction), 1.8 m wide (y-direction), and 1 m high (z-direction) test section. The water height, ζ, is nominally at $z = 0.5$ m. This is the surface reference elevation, i.e., $\zeta = 0$. Located at the upstream end of the test section is a two-phase active grid of mesh length $M = 100$ mm used to tailor the turbulent conditions in the air and water independently. A 2 m long wedge keeps the two phases separated at the beginning of the test section, allowing the turbulent flows to develop independently before they interact. This set-up facilitates the study of how a wide range of freestream turbulence intensities and Reynolds numbers affect the near-surface flow and surface topography.

Measurements were conducted at $x/M = 80$, which is sufficiently far downstream of the active grid to obtain quasi-homogeneous-isotropic regimes in the freestream of both phases (Comte-Bellot & Corrsin, 1966). The acquisition set-up was implemented to simultaneously capture two-dimensional, three-component (2D3C) flow fields on both sides of the interface as well as the surface topography. Velocity fields in horizontal planes (xy-planes) were captured using SPIV and the 3D surface topography using free-surface Fourier Transform profilometry (Cobelli *et al.*, 2009; Semati *et al.*, 2025). Here, u, v, and w denote velocities in the streamwise, spanwise (horizontal), and vertical directions, respectively. As the subsurface flow had to be visible to the SPIV cameras, the fluid could not be colored opaque, as is often done to get optimal profilometry results. Fluorescein is an organic dye with properties well-suited for the present use case. When used in the right concentration, the favourable emission spectrum of fluorescein allows for SPIV laser wavelengths to penetrate far enough into the flow field without substantially sacrificing profilometry quality. The SPIV measurement plane and profilometry locations are shown together with a photograph of the facility's test section in figures 1*a* and *b*.

Water-phase SPIV measurements were carried out using two LaVision Imager CX 25 megapixel cameras fitted with Sigma 105 mm focal length DG macro lenses. Illumination was provided by a dual-pulse Litron Nano L Nd:YAG laser with a wavelength of 532 nm, and the flow was seeded with neutrally buoyant polyamide (nylon) tracers with a nominal diameter of 40 µm. Each experimental case comprises three ensembles. For each ensemble, 600 image pairs were acquired at 15 Hz with a field of view of approximately 130×130 mm^2. Vector fields were processed using DaVis 10 with initial and final window sizes of 128×128 px^2 and 64×64 px^2, respectively, with 50 % overlap. The final water-phase SPIV vector spacing is 0.80 mm. In the air phase, two 4.5 megapixel Phantom T2540 high-speed cameras fitted with 300 mm focal length Nikon AF Micro Nikkor captured 20 000 image pairs at 1 kHz with a field of view of approximately 90×130 mm^2. SPIV vectors were calculated using initial and final window sizes of 96×96 px^2 and 48×48 px^2, respectively, resulting in a final vector spacing of 1.2 mm. The air-side planes were illuminated using a 532 mm dual-pulse Nd:YAG high-speed laser (Photonics DM 100-532 DH), and the flow was seeded with a water-based smoke fluid (JEM Pro-Fog Fluid) having droplets with a nominal diameter of 1 µm. A single Photron Fastcam Mini WX100 camera was used with a Nikon 60 mm focal length AF Micro Nikkor lens for profilometry measurements. The surface measurement data were acquired at the same frequency as the air-side SPIV, i.e., 1 kHz. All SPIV cameras were fitted with Scheimpflugs. For a graphical representation of the two SPIV planes, the profilometry surface topography planes and their relative positions, see figure 1*c*.

For each flow case, the streamwise centerline velocity, u_0 (subscript 0 denoting freestream variables), was measured via hot-wire anemometry. Data were acquired for 5 minutes with a sampling frequency of 75 kHz at the gas-phase channel half-height, $h = 0.25$ m measured from the nominal water height, i.e., $z = 0.75$ m from the channel floor. From these measurements, gas-phase integral scales, $\mathscr{L}_{11}$, were computed from an exponential fit of the velocity autocorrelation. The Kolmogorov microscale is defined as $\eta_0 = \nu_g^{3/4}\overline{\varepsilon}^{1/4}$, where ν_g is the gas kinematic viscosity, and $\overline{\varepsilon} = 15\nu_g\overline{(\partial u'/\partial x)^2}$ is the mean rate of dissipation of turbulent kinetic energy ($\bar{\cdot}$ denoting mean quantities). The Taylor microscale is estimated using $\lambda^2 = \overline{u'^2}/\overline{(\partial u'/\partial x)^2}$. All length scale estimates from hot-wire measurements rely on Taylor's frozen flow hypothesis, i.e., $U\partial/\partial x = \partial/\partial t$.

Additional gas-phase characterisation measurements were performed using a separate low-speed planar PIV set-up measuring u and w in a streamwise–vertical plane. Two LaVision MX 25S (25 megapixel) cameras provided a 200 mm wide stitched field-of-view covering the full height of the gas phase illuminated by the 532 nm low-speed laser. Acquisition frequencies were selected individually per case to ensure statistical independence between samples. From these measurements, the gas-phase bulk velocity is calculated from

$$U_b = \frac{1}{H}\int_0^H U(z)\mathrm{d}z,$$

excluding points in the immediate vicinity of the channel top-wall and gas-liquid interface. The gas-phase interface friction velocity, $U_{\tau,g} = \sqrt{(\tau/\rho)_g}$, where τ_g and ρ_g are the near-surface gas-phase shear stress and fluid density, respectively, is estimated from the near-interface shear stress ($\overline{u'w'}$) peak.

FLOW CHARACTERISTICS

The present study investigates flow cases with a moving airflow over a water-phase nominally at rest. Two active grid settings were used to produce different turbulent freestream conditions, here referred to as low (L) and high (H) freestream turbulence based on their relative freestream turbulence intensities $(u'/U)_0$, where U_0 is the freestream mean streamwise velocity and u'_0 the freestream velocity standard deviation. Flow cases are labelled according to the nomenclature T_{U_0}, where T denotes the freestream turbulence level (L or H). In the high freestream turbulence setting, the active grid operates in a fully random mode, whereas it is static with the grid rod winglets aligned with the flow in the low-turbulence setting. For each active grid setting, three Reynolds numbers, $Re_M = U_0 M/\nu_g$, were investigated. Gas phase flow parameters are listed in table 1. The turbulent Reynolds numbers based on the Taylor microscale and gas-phase interface friction velocity are $Re_\lambda = u'\lambda/\nu_g$ and $Re_\tau = U_{\tau,g}h/\nu_g$, respectively.

Also tabulated in table 1 are surface elevation statistics, including the mean deviation from the reference elevation, $\overline{\zeta}$. This is not equal for each experimental case due to head loss variation between flow conditions and the necessity to keep the water level at 0.5 m at the test-section's inlet wedge. The deviation also sets the mean distance between the horizontal SPIV planes and the surface. For the lowest airspeed ($U_0 \approx 4\,\mathrm{m/s}$), the air-side SPIV plane is located 15 mm above the nominal water height, whereas for all higher airspeeds, it is set to 30 mm. In all cases, the water-side SPIV planes are located 15 mm below the nominal water height. Thus, if $\overline{\zeta}$ is negative, the mean surface level is closer to the water-side SPIV planes, and vice versa. The wave amplitude, ζ_p, is taken from the r.m.s. of the profilometry surface elevation time series, $\zeta_p = \sqrt{2}\zeta_{\mathrm{r.m.s.}}$ and the peak wave frequencies, f_p, are taken from the surface elevation spectra summed over all measured streamwise wavenumbers k_x at spanwise wavenumber $k_y = 0$.

As previously discussed, changing the gas-phase Reynolds number can greatly impact the generated surface waves, and the present experiment is no exception. Though increasing Re_M generally leads to a monotonic increase in ζ_p and a decrease in f_p, the relationship is not strictly linear. What is interesting, however, is the high impact freestream turbulence has on wave statistics. Going from a turbulent Reynolds number of $Re_\lambda = 144$ to 315 whilst keeping Re_M relatively constant around 5×10^4 leads to an increase in r.m.s. wave amplitude of more than 40 %. A similar but opposite change is observed in the wave frequencies, suggesting that freestream turbulence has a pronounced effect on the formation of wind-driven waves. This result appears to be supported by the findings of Matas *et al.* (2015) despite the different methods of turbulence generation (bluff bodies and impinging jets versus an active grid).

INSTANTANEOUS DATA

Figure 2*a* depicts the streamwise instantaneous velocity, $u^+ = u'/U_{\tau,g}$, from an example SPIV snapshot for case L_8 featuring a region of low momentum flow (colored in blue) stretching across the field of view in the x-direction. A time series taken at a single x-value with a new x-axis reconstructed from Taylor's frozen flow hypothesis is shown in figure 2*b*. It features a long, meandering structure reminiscent of superstructures found in the logarithmic region of turbulent flat-plate boundary layers (Hutchins & Marusic, 2007). Such structures permeate the present datasets, stretching beyond $20h$ in the longitudinal direction for the lowest airspeed and freestream turbulence, becoming longer with increasing Re_M. As has been discussed by Hutchins & Marusic (2007) on the subject of boundary layer superstructures, the meandering nature of these streaks, coupled with a limited spanwise field of view, means their true length may be masked and thus underestimated by statistical quantities.

TWO-POINT CORRELATIONS

The two-point correlation coefficient, R_{AB}, between two quantities A and B is here defined as

$$R_{AB}(\Delta x, \Delta y) = \frac{\langle A'(x,y)B'(x+\Delta x, y+\Delta y)\rangle}{\sigma_A\sigma_B},$$

where $\langle\cdot\rangle$ denotes spatial means and $\sigma_{A,B}$ are standard deviations, and is calculated using Fourier transforms of A and B according to the cross-correlation theorem (Xu *et al.*, 2015). It provides a measure of how similar two quantities are to each other (or a single quantity to itself) as one is shifted spatially by lags Δx and Δy relative to the other. The contour plots in figure 3 show two-point correlations of streamwise, spanwise, and vertical gas-phase velocities for three Reynolds numbers, Re_M, at lower freestream turbulence.

The streamwise correlations, R_{uu}, (figure 3*a–c*) are virtually identical to those found in the logarithmic region of turbulent boundary layers (Hutchins & Marusic, 2007; Sillero *et al.*, 2014). In fact, when compared with horizontal PIV measurements over a flat-plate boundary layer experimental case from Hambleton *et al.* (2006) at $z/\delta = 0.087$ with $Re_\tau = 1100$, the case L_4, having similar parameters ($z/h = 0.081$, $Re_\tau = 3200$), presents a close to exact match. As freestream velocity increases, R_{uu}/h stretches in the streamwise direction, supporting the previous observation that the lengths of low-momentum streaks tend to increase with Re_M. Their width in the y-direction shows a similar trend, becoming increasingly wider with Re_M.

Figures 4*a–c* show the three velocity component two-point correlations shown in figure 3 as functions of $\Delta x/h$ along $\Delta y/h = 0$, together with two higher-freestream-turbulence cases (H_4 and H_8). Similarly, figure 4*d–f* depict two-point correlations as functions of $\Delta y/h$ along $\Delta x/h = 0$. From 4*a* and *d*, it is clear that changing freestream turbulence has a comparable effect to changing Re_M with R_{uu} extending farther in both streamwise and spanwise directions. These observations are in line with previous observations of turbulent boundary layers,

Table 1. Turbulent freestream statistics in the gas phase obtained from hot-wire data tabulated together with surface elevation statistics.

Flow case	Re_M	U_b	$(u'/U)_0$	$\mathscr{L}_{11}$	η	Re_λ	Re_τ	$\overline{\zeta}$	ζ_p	f_p
	[$\times 10^4$]	[m/s]	[%]	[mm]	[mm]			[mm]	[mm]	[Hz]
L_4	2.4	3.26	2.90	129	0.73	100	3200	−5.20	1.41	5.74
L_8	4.9	6.49	3.80	151	0.34	144	7600	−2.00	5.57	3.62
L_{10}	5.9	7.47	4.62	159	0.25	174	8500	0.14	8.29	2.98
H_4	2.5	3.33	6.52	261	0.49	241	3600	0.26	1.89	5.31
H_8	5.2	6.64	7.11	392	0.25	315	8800	−0.65	7.97	3.08
H_{10}	6.2	7.83	7.73	441	0.20	349	11100	−0.48	10.83	2.98

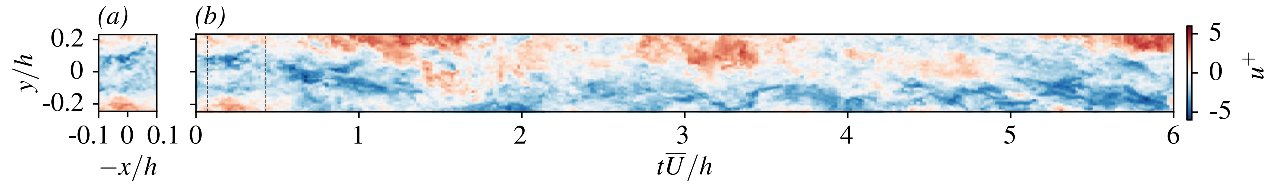

Figure 2. *(a)* A single snapshot of the gas-phase streamwise velocity, u^+, in the horizontal plane at $z/h = 0.128$ for the case L_8. *(b)* Horizontal-spanwise slices at a single x-location extruded in time with a new x-axis; reconstructed using Taylor's hypothesis based on the local mean $U = 4.67\,\mathrm{m/s}$. Dashed lines indicate the temporal location of the snapshot shown in *(a)*. Axes are equal in aspect ratio.

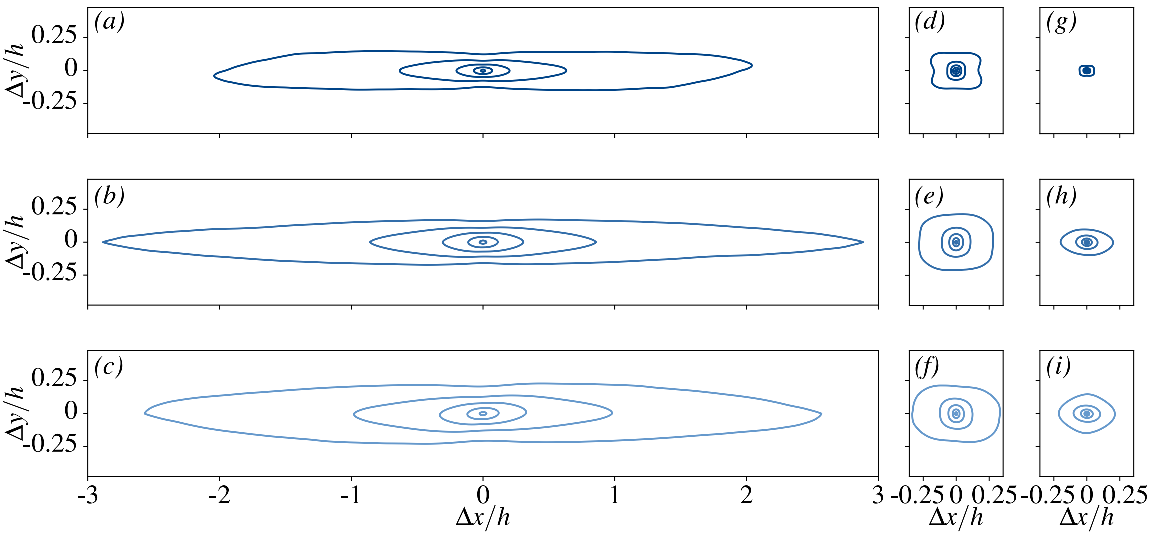

Figure 3. Two point correlations of (*a-c*) streamwise, R_{uu}, (*d-f*) spanwise, R_{vv}, and (*g-i*) surface-normal, R_{ww}, velocity components. Top row (*a, d, g*) corresponds to L_4, middle (*b, e, h*) corresponds to L_8 and bottom (*c, f, i*) corresponds to L_{10}. Contours show correlation values in the range $0.1 \leq R \leq 0.9$ with steps of 0.2. For R_{uu}, the x-axis is reconstructed from local mean velocities using Taylor's hypothesis. For R_{vv} and R_{ww}, the spatial correlations are taken directly. Distance from $\overline{\zeta}$ is $z/h = 0.081$ for L_4, 0.128 for L_8, and 0.119 for L_{10}.

where added freestream turbulence has the effect of maturing the boundary layer (Dogan *et al.*, 2017; Jooss *et al.*, 2021).

The two-point correlations of spanwise velocity, R_{vv}, depicted in figures 3*d–f* and 4*b* and *e* describe to what extent the sign of v stays constant in space, i.e., for how long a fluid parcel moves in the same spanwise direction before turning. Larger values of R_{vv} therefore point to higher rates of meandering behaviour. Compared to its streamwise counterpart, R_{vv} tends to zero at a much faster rate with Δx. However, the same trend, in which larger values of Re_M and freestream turbulence intensity lead to correlations extending farther in both streamwise and spanwise directions, is observed for R_{vv}, indicating increased meandering behaviour. Hutchins & Marusic (2007) suggested that this meandering behaviour masks the true size of superstructures in the log-region of turbulent boundary layers from single-point measurements, pointing to a characteristic X-shape found in the two-point correlation, R_{uu}, constructed from hot-wire rake data. Such a distinct shape is

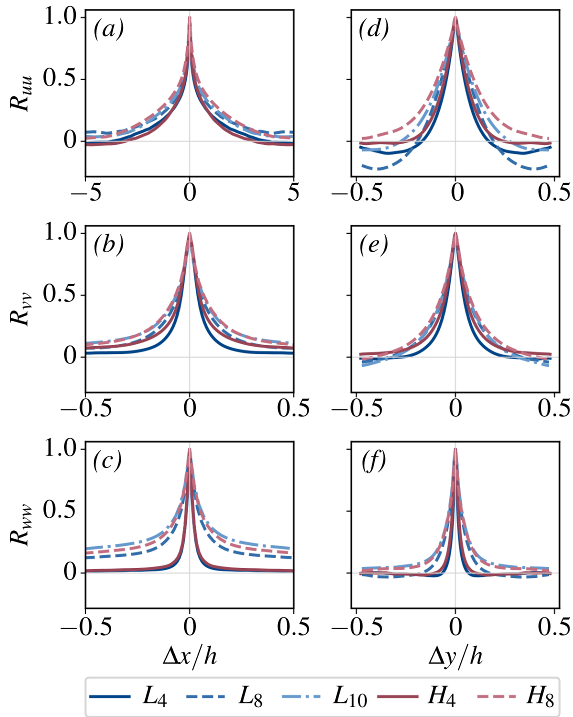

Figure 4. Streamwise ($\Delta y = 0$) and spanwise ($\Delta x = 0$) autocorrelations of streamwise (R_{uu}), spanwise (R_{vv}), and surface-normal (R_{ww}) velocity components. Note the larger Δx span in *(a)*.

not seen in the present data. However, this could be due to a number of factors, including the relatively short sampling time (three ensembles of 20 seconds) and the markedly different boundary conditions.

Finally, the vertical velocity two-point correlations, R_{ww}, give insight into the coherence between surface deformations and the gas-phase flow above it. In turbulent boundary layers and channel flows, two-point correlations of spanwise and vertical velocity are largely independent of Reynolds number (Sillero *et al.*, 2014). Here, we see the first clear difference between classical boundary layer turbulence and the present flow configuration, where correlations in w grow in both the streamwise and spanwise–horizontal directions as Re_M increases, and surface waves grow in wavelength. Buckley & Veron (2016) has shown that in the airflow above waves, especially young wind waves, flow separation produces intense wave-coherent turbulence. This is reflected in figure 5, showing increased coherence between vertical velocity fluctuations and surface elevation, $C_{w\zeta}$, around the peak wave frequency, f_p, for high-Re_M flow cases. The increase in length scales in R_{ww} is likely associated with ejections of low-momentum fluid downstream of wave crests growing in size as wave frequencies decrease. Flow separation events over wave troughs—which are not measured directly here, but commonly found in similar laboratory environments—are also a likely contributor to this coherence. At lower Re_M, the surface wave amplitudes, ζ_p, are much smaller, and the gas-phase vertical velocity power spectral densities shown in figure 5*b* show no trace of the peak wave frequencies from figure 5*c*. This is not to say that there is no wave-coherent turbulence in the flow at these lower Reynolds numbers, only that the effect is not seen at the measured height of the boundary layer.

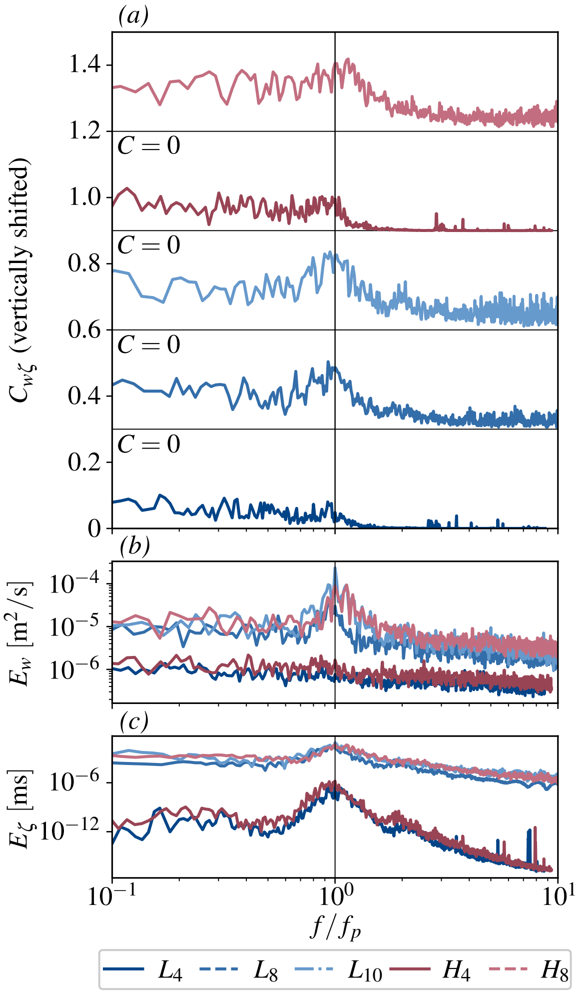

Figure 5. *(a)* Coherence between gas-phase vertical velocity fluctuations w' and surface deformation ζ, $C_{w\zeta}$, as functions of frequency normalised by f_p listed in table 1. Values of $C_{w\zeta}$ are vertically shifted by 0.3. Figures *(b)* and *(c)* show the power spectral densities of vertical velocity fluctuations in the near-surface gas phase and surface deformation, E_w and E_ζ, respectively.

CONCLUSION

The near-surface gas-phase and liquid-phase flow was measured in horizontal planes simultaneously with surface topography in a combined air-water channel facility. Several Re_M were investigated, and tailored turbulence was generated using an active grid. It is found that the turbulent structures present in the log-region of the near-surface gas phase boundary layer bear close similarities to the superstructures of flat-plate boundary layers. Analysis of two-point correlations in the *xy*-plane reveals similar behaviour for R_{uu} between the two, with length scales increasing with Re_M. Interestingly, a similar relationship, although smaller in magnitude, is found for spanwise-horizontal velocity correlations, R_{vv}, suggesting increased meandering behaviour at higher freestream velocities.

Another key finding is the relationship between freestream turbulence and surface-deformation amplitude and frequency. As expected, ζ_p increases with the gas-phase freestream velocity and wavelengths become longer with a decrease in peak frequency, f_p. A significant and comparable change in ζ_p and f_p is also observed with varying freestream turbulence, $(u'/U)_0$, proving that the turbulent characteristics of the wave-generating gas-phase flow are important to their development. Furthermore, high coherence between the log-region vertical gas-phase velocity, w', and the surface deformation, ζ, supports the idea that the longer streamwise tails in R_{ww} found at higher Re_M and $(u'/U)_0$, are due to low-momentum ejections from waves of lower frequency extending farther spatially.

ACKNOWLEDGEMENTS

Funded by the European Union (ERC StG 101041000, GLITR). Views and opinions expressed are, however, those of the authors only and do not necessarily reflect those of the European Union or the European Research Council. Neither the European Union nor the granting authority can be held responsible for them.

REFERENCES

Agrawal, Y. C., Terray, E. A., Donelan, M. A., Hwang, P. A., Williams, A. J., Drennan, W. M., Kahma, K. K. & Krtaigorodskii, S. A. 1992 Enhanced dissipation of kinetic energy beneath surface waves. *Nature* **359** (6392), 219–220.

Belcher, S. E. & Hunt, J. C. R. 1998 Turbulent flow over hills and waves. *Annu. Rev. Fluid Mech.* **30**, 507–538.

Buckley, M. P. & Veron, F. 2016 Structure of the airflow above surface waves. *J. Phys. Oceanogr.* **46** (5), 1377–1397.

Buckley, M. P., Veron, F. & Yousefi, K. 2020 Surface viscous stress over wind-driven waves with intermittent airflow separation. *J. Fluid Mech.* **905**, A31.

Cobelli, P. J., Maurel, A., Pagneux, V. & Petitjeans, P. 2009 Global measurement of water waves by Fourier transform profilometry. *Exp Fluids* **46** (6), 1037–1047.

Comte-Bellot, G. & Corrsin, S. 1966 The use of a contraction to improve the isotropy of grid-generated turbulence. *J. Fluid Mech.* **25** (4), 657–682.

Dogan, E., Hearst, R. J. & Ganapathisubramani, B. 2017 Modelling high Reynolds number wall–turbulence interactions in laboratory experiments using large-scale free-stream turbulence. *Philos Trans A Math Phys Eng Sci* **375** (2089), 20160091.

Hambleton, W. T., Hutchins, N. & Marusic, I. 2006 Simultaneous orthogonal-plane particle image velocimetry measurements in a turbulent boundary layer. *J. Fluid Mech.* **560**, 53–64.

Hutchins, N. & Marusic, I. 2007 Evidence of very long meandering features in the logarithmic region of turbulent boundary layers. *J. Fluid Mech.* **579**, 1–28.

IPCC 2023 Sections. In: Climate Change 2023: Synthesis Report. Contribution of Working Groups I, II and III to the Sixth Assessment Report of the Intergovernmental Panel on Climate Change [Core Writing Team, H. Lee and J. Romero (eds.)]. IPCC, Geneva, Switzerland. *Tech. Rep.*. Intergovernmental Panel on Climate Change (IPCC).

Jooss, Y., Li, L., Bracchi, T. & Hearst, R. J. 2021 Spatial development of a turbulent boundary layer subjected to freestream turbulence. *J. Fluid Mech.* **911**, A4.

Leibovich, S. 1983 The form and dynamics of Langmuir circulations. *Annu. Rev. Fluid Mech.* **15** (1), 391–427.

Li, T. & Shen, L. 2022 The principal stage in wind-wave generation. *J. Fluid Mech.* **934**, A41.

Matas, J.-P., Marty, S., Dem, M. S. & Cartellier, A. 2015 Influence of gas turbulence on the instability of an air–water mixing layer. *Phys. Rev. Lett.* **115** (7), 074501.

Miles, J. W. 1957 On the generation of surface waves by shear flows. *J. Fluid Mech.* **3** (2), 185–204.

Phillips, O. M. 1957 On the generation of waves by turbulent wind. *J. Fluid Mech.* **2** (5), 417–445.

Semati, A., Shankaran, A., Smeltzer, B. K., Æsøy, E., Hearst, R. J. & Ellingsen, S. Å. 2025 Simultaneous measurement of surface topography and subsurface velocity field in free-surface turbulent flow. Submitted manuscript, https://doi.org/10.48550/arXiv.2512.22641.

Shaikh, N. & Siddiqui, K. 2010 An experimental investigation of the near surface flow over air–water and air–solid interfaces. *Phys. Fluids* **22** (2), 025103.

Siddiqui, M. H. K., Loewen, M. R., Asher, W. E. & Jessup, A. T. 2004 Coherent structures beneath wind waves and their influence on air–water gas transfer. *J. Geophys. Res. C: Oceans* **109** (C3).

Sillero, J. A., Jiménez, J. & Moser, R. D. 2014 Two-point statistics for turbulent boundary layers and channels at reynolds numbers up to $\delta^+ \approx 2000$. *Phys. Fluids* **26** (10), 105109.

Thais, L. & Magnaudet, J. 1996 Turbulent structure beneath surface gravity waves sheared by the wind. *J. Fluid Mech.* **328**, 313–344.

Tondu, C., Gade, M., Morales Meabe, J. & Buckley, M. P. 2025 Wide-field-of-view PIV measurements above and below microscale breaking waves. *Exp Fluids* **66** (11), 200.

Veron, F. & Melville, W. K. 2001 Experiments on the stability and transition of wind-driven water surfaces. *J. Fluid Mech.* **446**, 25–65.

Xu, Y. F., Liu, J. M. & Zhu, W. D. 2015 Accurate and efficient calculation of discrete correlation functions and power spectra. *J. Sound Vib.* **347**, 246–265.